



Understanding Co roles towards developing Co-free Ni-rich cathodes for rechargeable batteries

Tongchao Liu¹, Lei Yu², Jiajie Liu³, Jun Lu^{®¹™}, Xuanxuan Bi¹, Alvin Dai¹, Matthew Li^{®¹}, Maofan Li³, Zongxiang Hu³, Lu Ma⁴, Duan Luo^{®²}, Jiaxin Zheng³, Tianpin Wu^{®⁴}, Yang Ren⁴, Jianguo Wen^{®²}, Feng Pan^{®³™} and Khalil Amine^{®¹,5™}

Current bottlenecks in cobalt (Co) supply have negatively impacted commercial battery production and inspired the development of cathode materials that are less reliant on Co. However, complete Co elimination is prevented by the lack of fundamental understanding of the impact of Co on cathode capacity and structural stability, as well as the lack of effective substitute components in practice. Here we investigate the roles of Co in purposely designed systems that include both Co-rich and Mn-substituted Co-free cathodes. Our results affirmed that Co plays an undeniable role in fast capacity and/or structural degradation, and found that Co is more destructive than Ni at high potentials, which offers unexpected but encouraging perspectives for Co reduction. Moreover, Mn substitution effectively alleviates the destructive effects of Co and enables a high potential functionality. With these fundamental discoveries, we demonstrated a series of LiNi $_{\alpha}$ Mn $_{\beta}$ X $_{\gamma}$ O $_{\alpha}$ (X = single or multiple dopants) as a promising candidate for Co-free cathodes.

s the automobile industry transitions towards electrification, rechargeable batteries must also meet the demands of the future. Although efforts to enhance battery performance have seen some success, they currently face a roadblock caused by high-cost constraints^{1,2}. These challenges with battery cost are primarily linked to skyrocketing prices and increased demand for transition metals (TMs), especially cobalt (Co) (ref. 3), which is a core material component in widely used commercial cathodes, such as LiCoO₂, LiNi_xMn_yCo_{1-x-y}O₂ and LiNi_{0.8}Co_{0.15}Al_{0.05}O₂ (refs. 4-6). In recent years, Co has become economically unattractive due to increased mining royalties, as well as political and ethical turmoil in Africa7. In response to these cost pressures, efforts have been made to develop low Co and even Co-free cathodes without trade-offs in battery performance. Although several possible alternatives, which include Li-and Mn-rich cathodes, high-voltage spinel LiNi_{0.5}Mn_{1.5}O₄ and disordered rock salt, have been highlighted as viable replacements for Co-containing cathodes⁸⁻¹¹, they possess impractical capacities and stability for large-scale commercial use¹². Hence, current research into low Co reliance remains largely centred on layered oxide cathodes¹³.

Ni-rich layered oxide cathodes can achieve a high capacity and energy density¹⁴⁻¹⁶. However, direct replacement of Co with Ni, such as in the case of LiNiO₂, has been confirmed to be practically infeasible due to notable reductions in battery performance and thermal stability¹⁵. Therefore, the search for effective substitute elements is the primary challenge for reducing Co use. A logical path towards replacing or reducing Co has to begin with understanding why Co is crucial within layered oxide cathodes². It is generally accepted that Co suppresses structural defects by reducing the Li/Ni disorder in Ni-rich compositions and achieves a well-crystallized layered

structure¹⁷. This helps to ensure the rate capability of Ni-rich cathodes, but the impact on the structural stability during cycling remains unclear. Fundamentally, it is understood that synergistic effects between Co, other TMs and lattice O not only determine intrinsic structural features, but also influence the structural transformation of Ni-rich cathodes during charge/discharge. In addition, owing to the overlap of the O and Co redox potentials, Co, in fact, deleteriously promotes a high lattice O activity (at high charge potentials), which results in oxygen release and irreversible phase transition¹⁵. As a high Ni content is widely viewed as the root cause of capacity degradation¹⁸⁻²⁰, the impacts of Co on the structural transformation and lattice O stability have not been much investigated in Ni-rich cathodes, despite their close relationships in electrochemical performance. Correlations between Co-related cation mixing and the dynamic structural stability of Ni-rich materials are similarly unclear. To properly develop Co-free cathodes or determine adequate component substitutes, a complete understanding of Co's functionality in Ni-rich cathodes is required.

In this work, Co-rich LiNi_{0.6}Co_{0.4}O₂, Mn-substituted Co-free LiNi_{0.6}Mn_{0.4}O₂ and commercially comparable LiNi_{0.6}Mn_{0.2}Co_{0.2}O₂ compositions were designed to elucidate the interplay between Co content, structural properties and capacity degradation in Ni-rich cathodes. The gathered evidence clearly shows that Co is, in fact, even more destructive than Ni at a high potential. Owing to the suppression of the Li/Ni disorder, Co exacerbates lattice parameter changes and promotes the formation of intragranular microcracks. Meanwhile, Co excessively activates an irreversible lattice oxygen redox, which induces oxygen release and irreversible structural transformations. These morphological and structural degradation mechanisms cumulatively result in a rapid capacity fade observed

¹Chemical Sciences and Engineering Division, Argonne National Laboratory, Lemont, IL, USA. ²Center for Nanoscale Materials, Argonne National Laboratory, Lemont, IL, USA. ³School of Advanced Materials, Peking University Shenzhen Graduate School, Shenzhen, China. ⁴X-ray Science Division, Argonne National Laboratory, Lemont, IL, USA. ⁵Material Science and Engineering, Stanford University, Stanford, CA, USA. [™]e-mail: junlu@anl.gov; panfeng@pkusz.edu.cn; amine@anl.gov

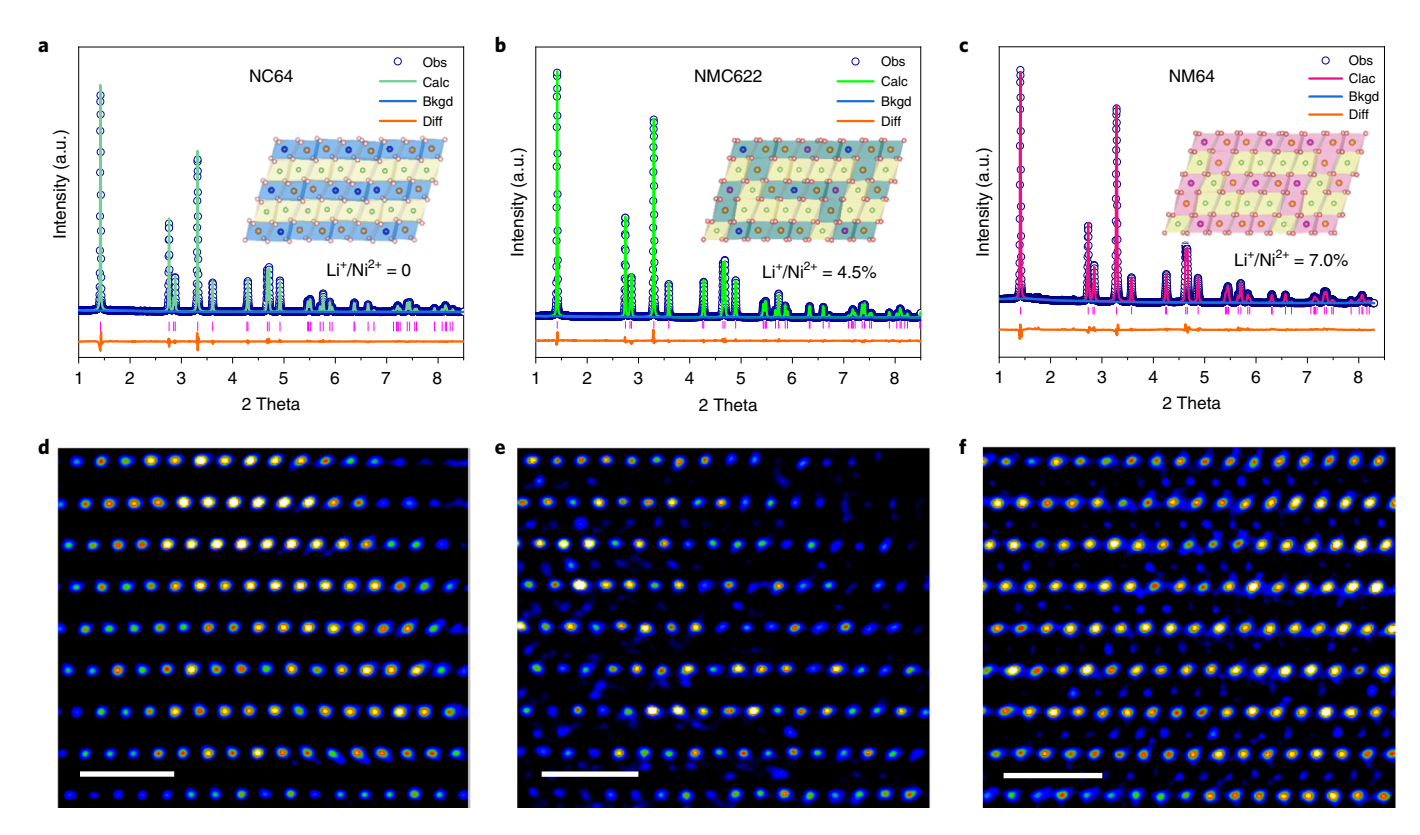


Fig. 1 | Quantitative atomic occupancy analysis via HEXRD refinements and aberration-corrected high-resolution TEM. a-c, HEXRD diffraction and Retvield refinement of NC64 (a), NMC622 (b) and NM64 (c) powders. The Li/Ni disorder ratios of NC64, NMC622 and NM64 were 0, 4.5 and 7.0%, respectively. Insets: corresponding structures with different Li/Ni disorders. **d-f**, High-resolution TEM images with atomistic level observations of NC64 (d), NMC622 (e) and NM64 (f) powders. The bright columns with the uniform arrangement should be arranged as TMs, and the dark columns between the TMs' columns should be arranged as Li layers. Scale bars, 1nm. a.u., arbitrary units.

in Co-rich cathodes. However, Mn substitution in Co-free cathodes contributes to stabilization of the lattice oxygen and suppression of the irreversible phase transitions during cycling. Despite an increase in the Li/Ni disorder in the Mn-substituted oxide, these results demonstrate that Ni-rich (also Co-free) cathodes are capable of high-voltage operations. Inspired by these in-depth insights, we postulated that LiNi $_{\alpha}$ Mn $_{\beta}$ X $_{\gamma}$ O $_{2}$ is a viable candidate for Co-free cathodes, as opposed to current research efforts that emphasize LiNiO $_{2}$ Co-free cathodes and Li- and Mn-rich cathodes. We also designed a series of Co-free cathodes with an enhanced performance as a tandem research direction for next generation, low cost and long calendar life batteries in widespread applications.

The role of Co on structures and performances

Three comparable Ni-rich layered oxide cathodes with compositions of $\mathrm{LiNi}_{0.6}\mathrm{Co}_{0.4}\mathrm{O}_2$ (denoted as NC64), $\mathrm{LiNi}_{0.6}\mathrm{Mn}_{0.4}\mathrm{O}_2$ (denoted as NM64) and $\mathrm{LiNi}_{0.6}\mathrm{Mn}_{0.2}\mathrm{Co}_{0.2}\mathrm{O}_2$ (denoted as NMC622), were synthesized using a co-precipitation method (Methods). These were designed to simultaneously investigate the intrinsic properties that arise from Co content and the potential effect of Mn on Ni-rich layered oxide cathodes. NMC622 was selected as the control sample due to its moderate composition.

The analysis of compositions and morphology is described in the Supplementary Table 1 and Supplementary Fig. 1. The structure and atomic occupancy were further analysed by high-energy X-ray diffraction (HEXRD). As shown in Fig. 1a–c and Supplementary Table 2, Co-rich NC64 exhibited Li and TMs that, respectively, occupied the 3a and 3b sites, which provided a near-perfect layered structure with almost no Li/Ni disorder. It is consistent with our previous results that Co³+ is capable of reducing the Li/Ni disorder

by suppressing the magnetic frustration and superexchange intercalations^{21–24}. By reducing Co via Mn substitution to form NMC622, the Li/Ni disorder noticeably increased to 4%. Complete replacement of Co with Mn in NM64 further increased the Li/Ni disorder to at least 7%. It is reasonable that a strong magnetic frustration present in Ni²⁺/Ni³⁺ and Mn⁴⁺ and the superexchange intercalations between the TMs and antisite Ni²⁺ (in Li layers) promoted an increased Li/Ni disorder in a Co-free cathode²⁰. Based on these results, it is clear that Co is effective in suppressing the formation of Li/Ni disorder. In contrast, Mn in a Ni-rich cathode is prone to form Li/Ni disorder, which can be further tuned to some extent by regulating the calcination temperature to optimize the Li/Ni disorder.

Aberration-corrected high-resolution transmission electron microscopy (TEM) images confirmed the typical layered structures of the three samples. As shown in Fig. 1d, no bright spots were visually captured in the Li layers, which verifies that the Li/Ni disorder was negligible for the NC64 sample. When the atomic-level inspection was done on the NMC622 sample (Fig. 1e), we found a small number of weak signals in the Li layers, which suggests the existence of Li/Ni disorder in NMC622. A similar examination conducted on the NM64 samples showed that Li/Ni disorder abundantly occurred in NM64 (Fig. 1f). These atomistic observations from TEM combined with the X-ray diffraction (XRD) refinement results indicate that Li/Ni disorder decreases with increasing Co content, but increases with increasing Mn content.

Given the apparent structural differences of the as-prepared samples, it was of particular interest to explore correlations between different Co/Mn contents, the resulting structural properties and their electrochemical performance. As shown in Fig. 2a, the initial

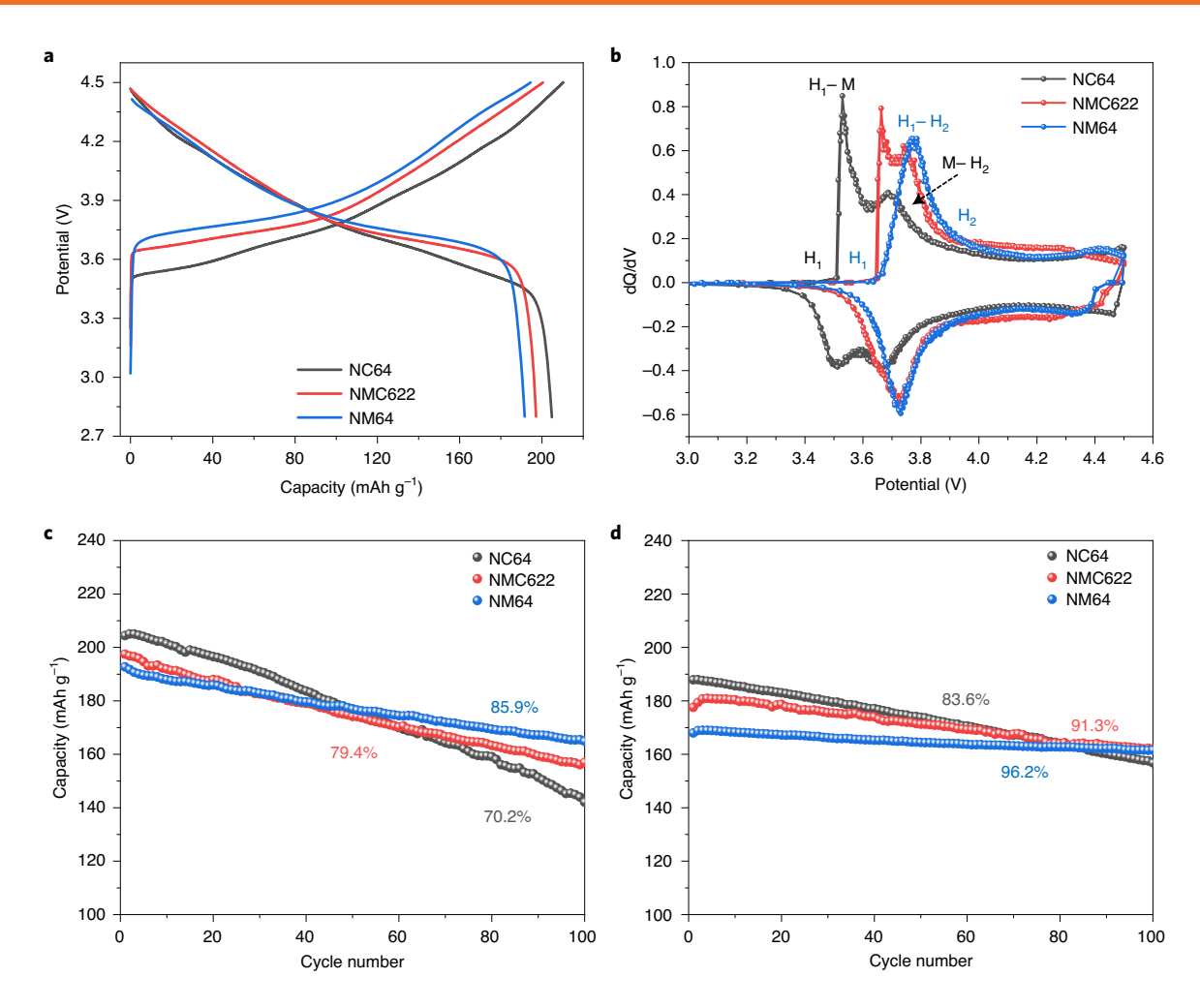


Fig. 2 | **Electrochemical measurements of NC64, NMC622 and NM64. a**, Charge/discharge curves of NC64, NMC622 and NM64 with voltage ranges of 2.8-4.5 V at a current rate of 0.1C. **b**, The dQ/dV curves of NC64, NMC622 and NM64 at a current rate of 0.1C. The phase-transition processes are labelled. **c**, Cycle performance of these comparable samples at a current rate of 0.1C with a cutoff voltage of 4.5 V. The capacity retentions of NC64, NMC622 and NM64 were 70.2, 79.4 and 85.9%, respectively. **d**, Cycle performance of these comparable samples at a current rate of 0.1C with a cutoff voltage of 4.3 V. The capacity retentions of NC64, NMC622 and NM64 were 83.6, 91.3 and 96.2%, respectively.

discharge capacities at a current rate of C/10 were 205, 197 and 191 mAh g⁻¹ for NC64, NMC622 and NM64, respectively. The difference in capacity between these three materials was ascribed to their different degree of Li/Ni disorder, as Ni²⁺ and Li⁺ antisites are both electrochemically inert²⁵. Despite its lower reversible capacities, NM64, with a higher average voltage, beneficially increased the overall energy density. As shown in Fig. 2b, the dQ/dV curves of NC64 and NMC622 both show two sharp peaks at 3.6–3.7 V, which correspond to two phase-transition processes (from phase H₁ to the M phase, and from phase M to the H₂ phase)²⁶. However, Co-free NM64 only shows a single broad peak, which indicates a smooth single phase transition. Figure 2c shows the capacity retentions over 100 cycles, which were recorded as 70.2, 79.4 and 85.9% for NC64, NMC622 and NM64, respectively, when operated within a voltage range of 2.8-4.5 V. NC64 showed severe capacity degradation at this voltage range. The synchronous decay in all the dQ/dVpeaks of NC64 and the quickly increased charge-transfer resistance indicate an irreversible structural transformation (Supplementary Figs. 2 and 5a). With decreases in the Co content and the appearances of Li/Ni disorder, the cycling performances and structural reversibility of NMC622 and NM64 exhibited clear upward trends (Supplementary Figs. 3-6), which was evident even when the charge rates were increased. Figure 2d shows that the capacity retentions of NC64, NMC622 and NM64 remained at 83.6, 91.2 and 96.2% within a lower voltage range of 2.8-4.3 V, respectively, which indicates an apparent improvement of the cycling stabilities compared with that in the voltage range 2.8-4.5 V, especially for NC64. Initially, the capacity degradation mechanism of Ni-rich cathodes was predominately attributed to a high Ni content, whereas the effects of Co and Mn were blurred due to their relatively low content and low operating voltage¹⁵. Based on the cycle stability comparisons here, it was confirmed that Co and Mn notably affect the electrochemical performance. Co appears to be detrimental to the cycle stability and structural reversibility of Ni-rich cathodes, particularly at a high potential. Mn substitutes, with more Li/Ni disorder, exhibit a noticeable improvement in capacity retention and structural reversibility. We further compared the thermal stability of these three samples through differential scanning calorimetry (Supplementary Fig. 7). Unsurprisingly, thermal stability shows an upward trend with a Co reduction and Mn increase. Thus, an in-depth understanding of the Co and Mn properties will be of great significance to fulfil knowledge gaps.

To further build or our understanding of the structural property effects that originate from different Co/Mn contents on the electrochemical performance, in situ HEXRD measurements were performed on NC64, NMC622 and NM64. The Bragg reflections

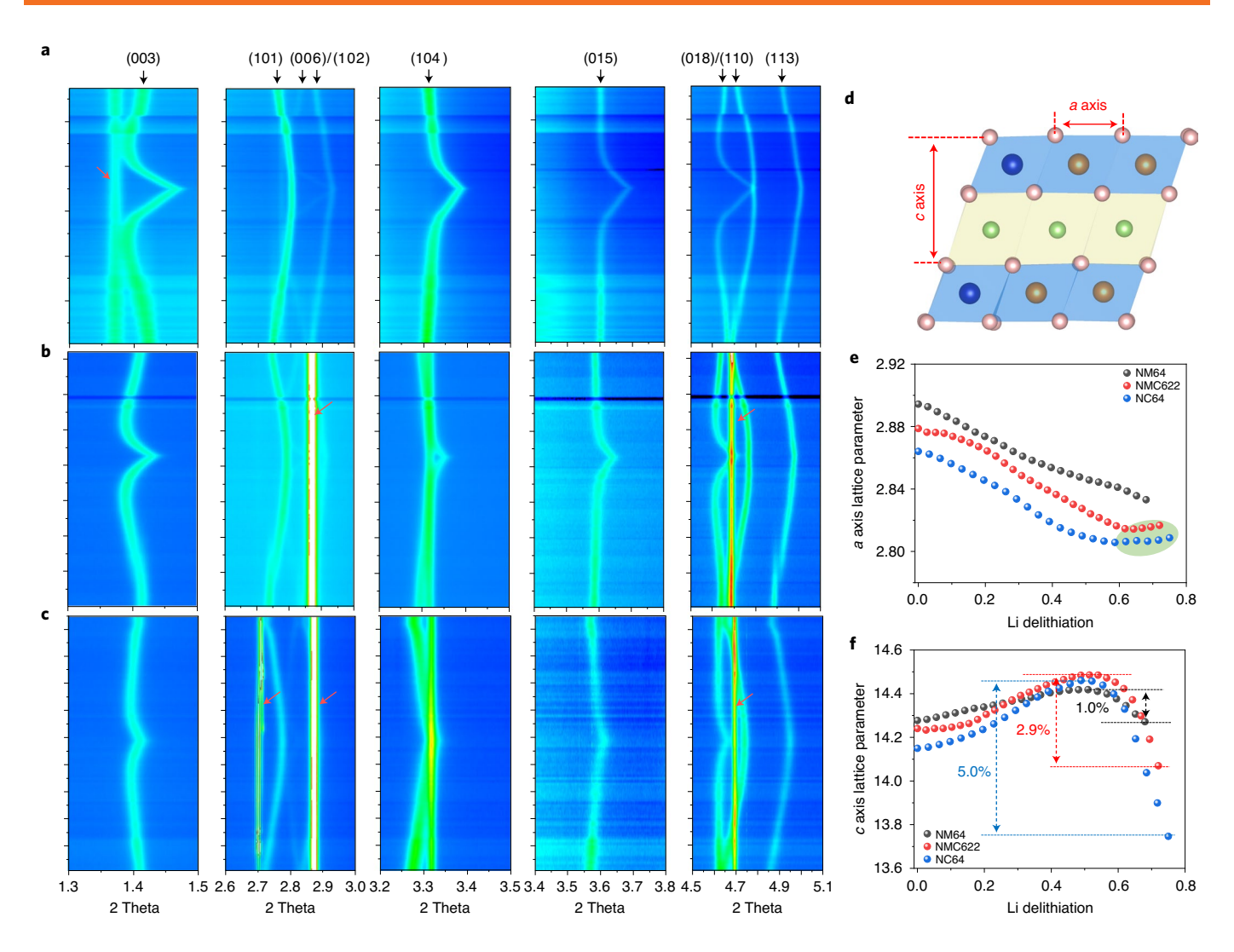


Fig. 3 | In situ synchrotron HEXRD characterization during the first charge/discharge. a-c, Two-dimensional contour plots of in situ XRD during the structural evolution of NC64 (a), NMC622 (b) and NM64 (c) cathodes. Some impurities in the XRD curve are labelled by red arrows and explained in Supplementary Figs. 9, 11 and 13. **d**, Schematic diagram with typical lattice parameters of layered oxide materials. **e**, The *a*-axis lattice parameter changes in the as-prepared samples obtained from Rietveld refinements. **f**, The *c*-axis lattice parameter changes in the as-prepared samples obtained from Rietveld refinements. The lattice changes of the *c* axes of NC64, NMC622 and NM64 were 5.0, 2.9 and 1.0%, respectively.

indicate that the structural evolutions in the three cathodes during charge-discharge were quite different. As shown in Fig. 3a and Supplementary Figs. 8 and 9, NC64 exhibited clear structural evolutions, wherein most of the diffraction peaks shifted markedly with delithiation/lithiation. Initially, the visible phase transition from M to H₂ was tracked by the [110] and [113] peaks in the NC64 sample, which corresponded to the second peak of dQ/dV at 3.7 V. Based on the fast degradation of the dQ/dV peaks (Supplementary Fig. 2), this phase transition was not reversible and resulted in a rapid capacity fade. After entering the H2 phase, the [003] peak starts to shift left and reaches a local maximum at 4.25 V, which suggests that the interlayer space increased with electrostatic repulsion²⁶. Afterwards, the [003] peak markedly shifted right to 4.5 V, which corresponds to a phase transition from H₂ to H₃ with a rapidly reduced interlayer spacing. Such sharp changes in the lattice parameters will damage the particle morphology in the form of intragranular and intergranular microcracks. During discharge, the structural evolution of NC64 followed the reverse transformation sequence. However, it is especially noteworthy that most peaks deviated from their original 2θ positions after the first cycle, which indicates that an irreversible structural evolution occurred during the first cycle. Such variations

would adversely accumulate on long-term cycling, and eventually lead to structural degradation and capacity fade.

NMC622 shows similar phase transition processes, but with enhanced reversibility. Left/right [003] peak shifts related to lattice expansion/contraction were noticeably weaker than those in NC64 (Fig. 3b and Supplementary Figs. 10 and 11). However, it is evident that NMC622 had a more symmetric structural evolution during the first charge-discharge cycle, in which most of the diffraction peaks returned to their original 2θ positions. Compared with NC64 and NMC622, NM64 experiences a quite different structural evolution process. For NM64, the phase transition from H1 to H2 was smooth (Fig. 3c and Supplementary Figs. 12 and 13) with slight peak shifts, and the intermediate M phase was completely absent, whereas abrupt peak jumps were observed in NC64 and NMC622 during the initial charge process. Lattice expansion and/or contraction was naturally present in highly delithiated NM64, but in this case showed only trivial changes. During discharge, NM64 fully reverted back to the initial structure, and so exhibited a highly reversible phase-transition process.

The Rietveld refinements for in situ XRD data were performed to quantitatively analyse the lattice parameter variation of the

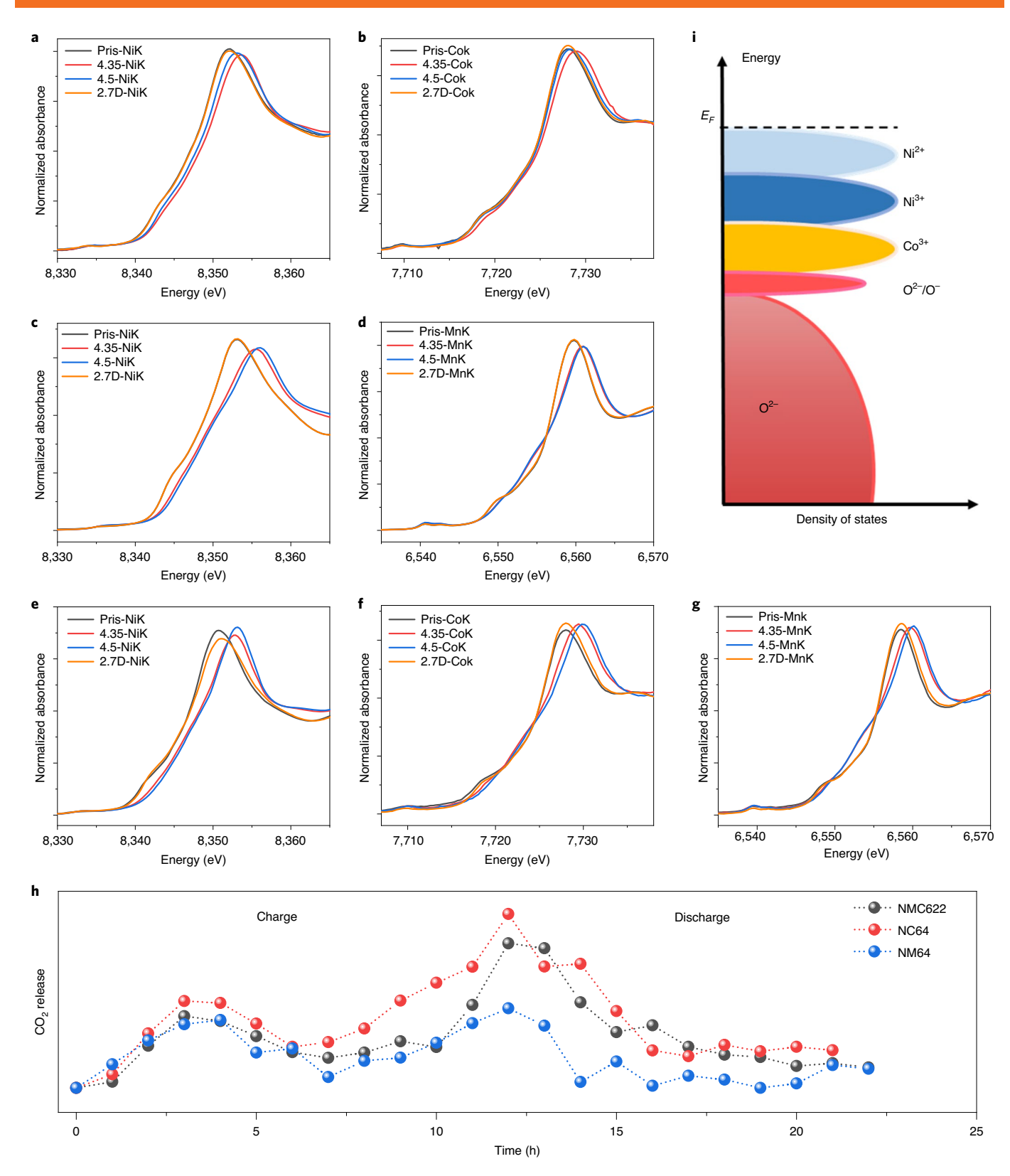


Fig. 4 | TM oxidation states and gas-generation measurements for three comparable samples. **a,b**, Ex situ Ni (**a**) and Co (**b**) K-edge X-ray absorption near edge structure (XANES) spectra of an NC64 sample. **e,c**, Ex situ Ni (**c**) and Mn (**d**) K-edge XANES spectra of an NM64 sample. **e-g**, Ex situ Ni (**e**), Co (**f**) and Mn (**g**) K-edge XANES spectra of an NMC622 sample. 2.7D refers to the discharge voltage. **h**, In situ differential electrochemical mass spectroscopy measurements for NC64, NM64 and NMC622. **i**, Density of states schematic diagram of TMs and O.

as-prepared samples. As shown in Fig. 3d,f, the $\it c$ axis lattice parameters of the three samples exhibit distinct trends in expansion and contraction. NC64 especially shows a considerable lattice parameter

change of over 5%. Such a large structural expansion and contraction can potentially cause particle morphological damage in the form of intragranular microcracks²⁷. With decreasing Co content,

NMC622 exhibits a smaller lattice-parameter change around 2.9% and Co-free NM64 shows the smallest lattice parameter change of less than 1%. The suppression of the lattice parameter changes in NM64 arises from Li/Ni disorder that builds a 'bearing beam' in the layered structure frame. Our in situ XRD data clearly confirmed, yet again, that Co inevitably induces a fast structural degradation as a consequence of exacerbating the structural transformation. Reducing Co content by Mn substitution significantly enhances structural reversibility and weakens variation in the lattice parameter due to the positive effects of the optimized Li/Ni disorder on structural stabilization, as highlighted in the XRD results.

To further verify the detrimental effects of Co in Ni-rich cathode materials, we designed LiNi_{0.8}Co_{0.2}O₂ (NC82) with a similar single-particle morphology and 1.9% Li/Ni disorder (Supplementary Figs. 14 and 15, and Supplementary Tables 3 and 4). Surprisingly, the cycle stability of NC82 was superior to that of NC64, which deviates from the current theory, in which high Ni content is the root cause of structural degradation and debilitating electrochemical performance (Supplementary Fig. 16)28. In addition, in situ XRD results revealed that lattice expansions/contractions obviously weakened in the NC82 sample, which was attributed to the low Co content and the pillar function of Li/Ni disorder (Supplementary Figs. 17-19). Based on the comparison of NC64 and NC82, we verified that Co-rich contents deteriorated the structural stability of layered oxide cathodes, and were even more destructive than Ni at high potentials. Moreover, the benefits of Li/Ni disorder to structural stability were reaffirmed.

Cationic and anionic redox in Ni-rich cathodes

The fact that Co promotes excessive lattice contraction at high potentials will inevitably affect O redox. Despite providing additional capacity, O redox has been considered to be a partially irreversible reaction that leads to the Ni-rich cathode structural instability^{29,30}. It often links to the changes in the lattice parameter along the a/baxis, the oxygen-oxygen (O-O) bond lengths and the oxidation states of TMs. Figure 3d,e shows that a/b axis lattice parameters decrease with delithiation, which indicates synchronous reductions in the O-O bond length and TM oxidation. Unexpectedly, it was observed that the a/b axis lattice parameters of NC64 and NMC622 remained constant and even exhibited slight increases with further delithiation at high potentials, especially for NC64, which are deviations from the conventional TM reduction reactions. As voltage increased, electrons were continuously released from redox centres (either TM^{n+} or O^{2-}). Therefore, the deviations in the TM reduction provide evidence that O was involved in the redox at high potentials because its redox activity overlaps with Ni3+/4+ and Co3+/4+ pairs (Fig. 4i). Likewise, the shortening of the O-O bond has been reported to activate O to participate in the redox reaction³¹. The fact, that the O-O bond length of NC64 initially shrank and then stayed the same further verifies the occurrence of O redox.

X-ray absorption spectroscopy (XAS) was applied to track the oxidation state changes of the three samples. Figure 4a,b shows that the oxidation states of Ni and Co simultaneously increased with Li extraction in NC64. The concurrent valence changes of Ni and Co were affirmed by density functional theory calculations, as shown in Supplementary Fig. 20a,b. More interestingly, the valence state of Ni and Co consistently reached the maximum at a charged potential of 4.35 V, and then unexpectedly decreased at the end of the charge (4.5 V). This result is consistent with the in situ XRD refinements discussed above. The aberrant reduction of Ni and Co further confirmed that the lattice O served as a redox centre at high potentials. Compared with that of NC64, oxygen stability gradually improved with Co reduction and Mn increase in NMC622 and NM64. Figure 4c,d shows that the oxidation state of Ni in NM64 continuously increased but Mn remained constant during the whole charge process, which is also consistent with density functional

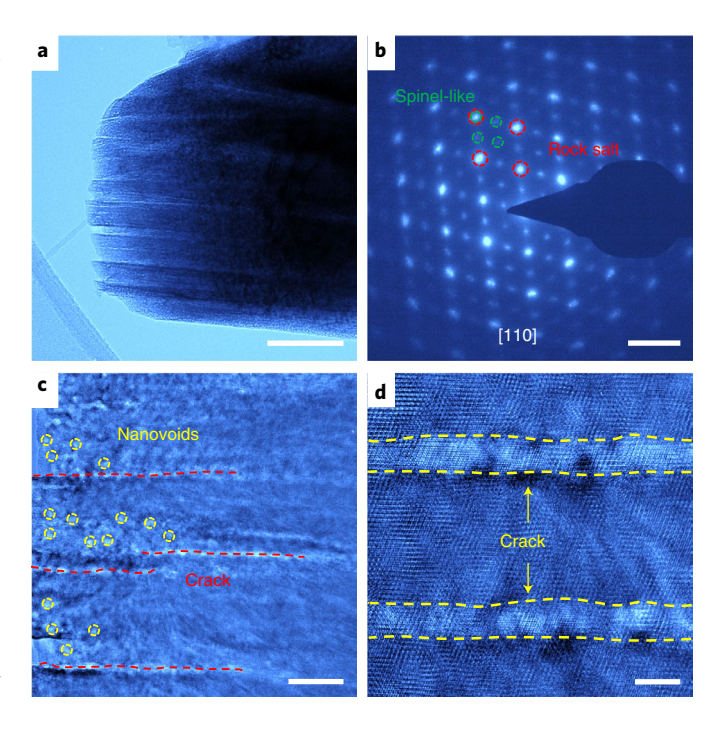


Fig. 5 | TEM observations of NC64 after cycling. a, Low magnification TEM image of NC64 after 100 cycles. **b**, Selected area diffraction image of NC64 along the [110] direction. **c**, High magnification TEM image of NC64 after cycling. **d**, High-resolution TEM image of NC64 after cycling. Scale bar, 100 nm (**a**), 5 nm⁻¹ (**b**), 20 nm (**c**) and 5 nm (**d**).

theory calculations (Supplementary Fig. 20c,f). NMC622 is expected to show slight decreases in TM valance at 4.5 V as a tiny increase in the O–O bond length was observed from XRD refinement at the end of charge. However, this was not captured in ex situ XAS (Fig. 4e–g) because the valance reduction of Ni in NMC622 may be very limited when compared with that in NC64. These results illustrate that O redox was effectively suppressed by reducing Co with Mn substitution.

Operando differential electrochemical mass spectrometry was carried out to directly investigate whether the redox of lattice O was reversible. First, there was no evidence of direct O₂ generation during the charging process, with only a small amount of CO₂ detected. As shown in Fig. 4h and Supplementary Fig. 21, the three cathodes consistently showed onsets of CO₂ evolution at lower potentials due to the oxidation of carbonate impurities²⁹. CO₂ generation occurred earlier and in greater quantities than in NC64 at high potentials, which indicates that the lattice O was excessively active and reactive with the electrolyte. As the Co content decreased, CO₂ generation also reduced in NMC622 and NM64. When combined with in situ XRD and ex situ XAS, these differential electrochemical mass spectrometry results verified that at least part of the O redox in the Co-rich composition was irreversible, whereas reducing Co with Mn substitutes enhanced the Co by oxygen stability.

Morphology and structural degradation

Morphological observations by TEM showed that intragranular cracks were observable along the *c* axis of the NC64 single particle (Fig. 5a). Intragranular cracking due to huge lattice parameter changes caused not only mechanical failure, but also structural degradation under severe electrochemical conditions^{32–34}. In addition, the detection of a large number of nanovoids inside the NC64 single particles provided direct evidence of oxygen release (Fig. 5c). High-resolution TEM images (Fig. 5d) with selected area diffraction (Fig. 5b) demonstrated that the bulk structure of NC64 almost

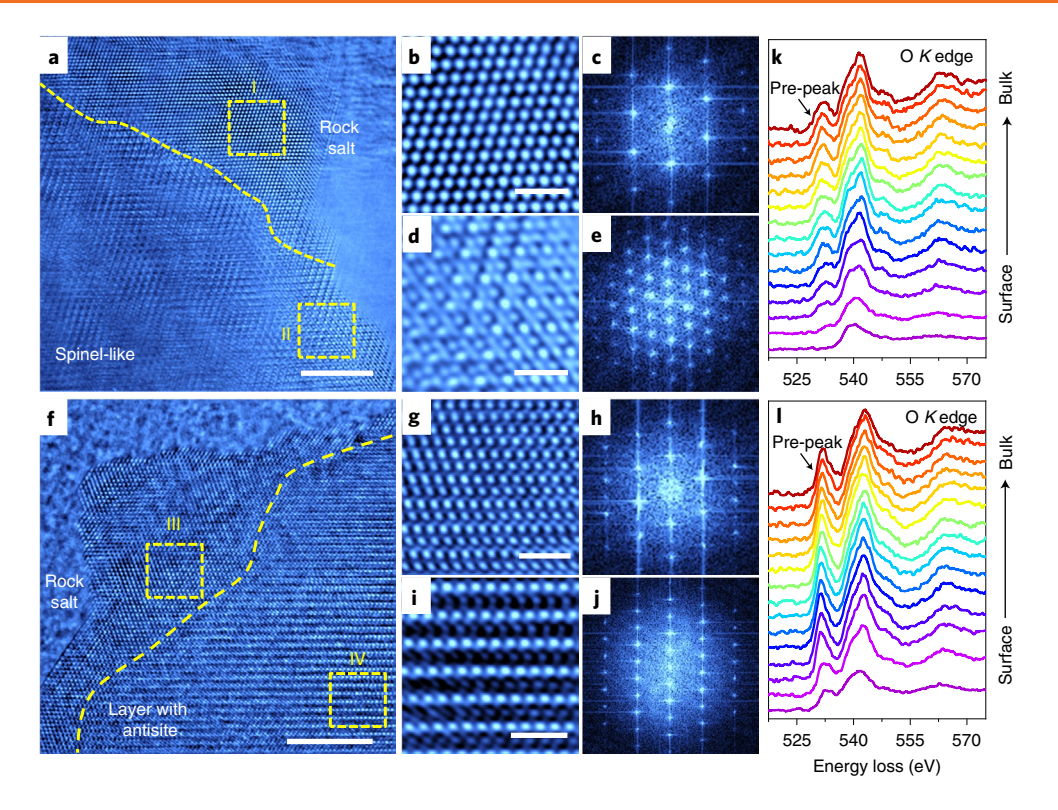


Fig. 6 | Structure and oxygen reversibility for NC64 and NM64. a, High-resolution TEM image showing the atomic surface structure of NC64. **b,c**, Enlarged figure (**b**) and fast Fourier transform (FFT) image (**c**) of a selected area (I) in **a. d,e**, Enlarged figure (**d**) and FFT image (**e**) of a selected area (II) in **a. f**, High-resolution TEM imaging showing the atomic surface structure of NM64. **g,h**, Enlarged figure (**g**) and FFT image (**h**) of a selected area (III) in **f. i,j**, Enlarged figure (**i**) and FFT image (**j**) of a selected area (IV) in **f. k,l**, Electron energy-loss spectroscopy line scans of the O K edge in cycled NC64 (**k**) and NM64 (**l**). Scale bars, 5 nm (**a,f**), 1 nm (**b,d,g,i**).

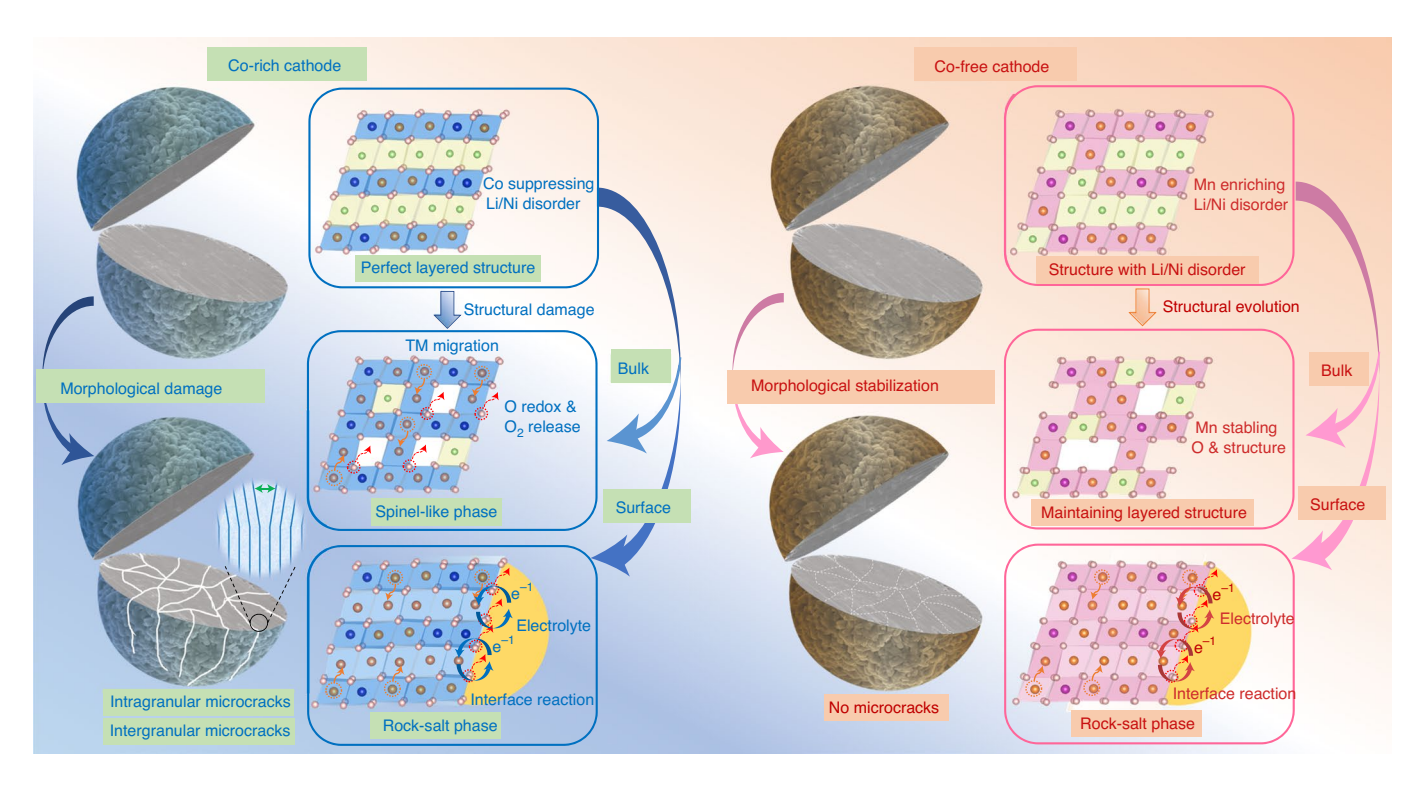


Fig. 7 | Structural evolution mechanisms for Co-rich and Co-free cathodes. a, In the Co-rich cathode, Co suppressed the formation of Li/Ni disorder. During cycling, Co triggered more severe morphological damage and structural degradation, such as TM migration and oxygen release. **b**, Co-free cathodes with Mn substitution had more Li/Ni disorder. During cycling, Co-free cathodes exhibited better structural and/or morphological stability and suppressed oxygen release. The surface phase transformation from the layer structure to the rock-salt phase was independent of the Co and Mn composition.

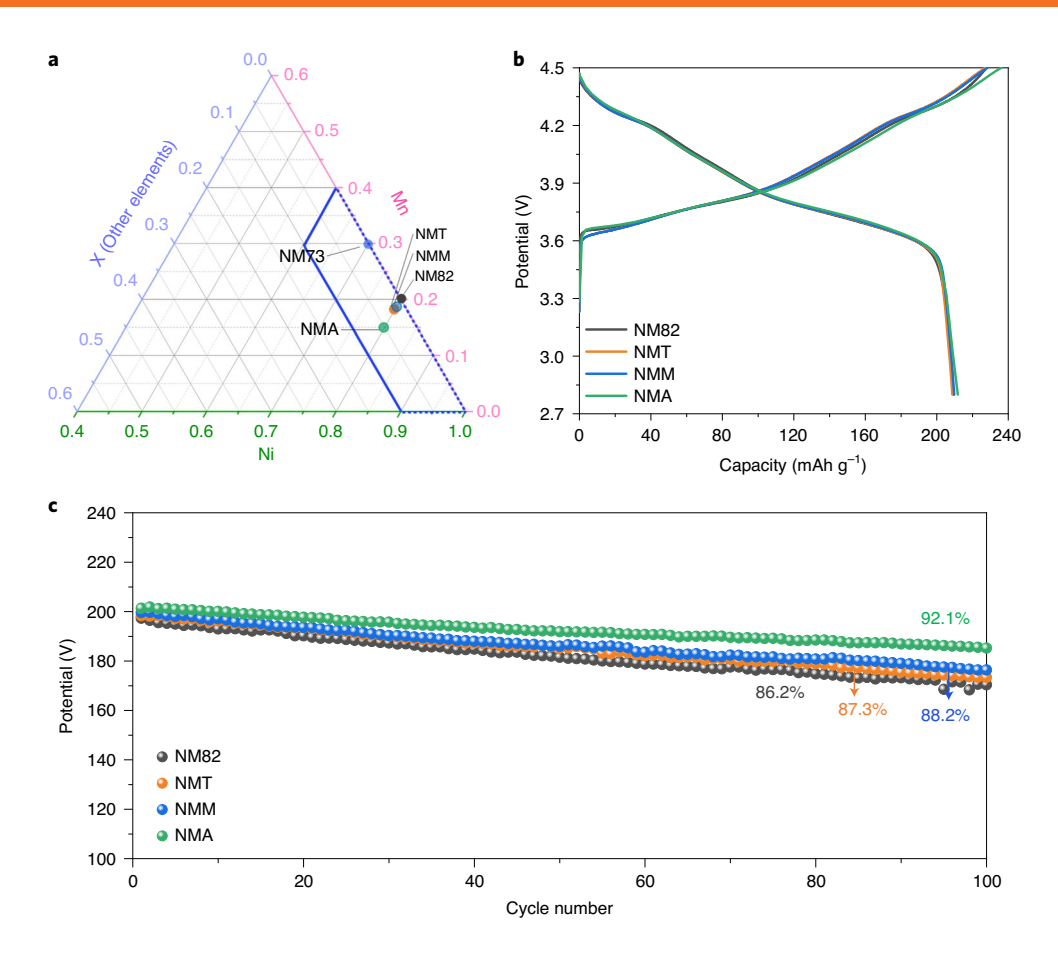


Fig. 8 | Prospective Co-free LiNi_αMn_βX_γO₂ **cathode materials. a**, Compositional phases of prospective Co-free cathode materials. The trapezoid part represents the potential composition of Co-free cathodes, in which Ni \geq 0.6, Mn \leq 0.4 and X \leq 0.1. The figure includes some successful examples reported in the text. **b**, Charge/discharge profiles of NM82, NMT, NMM and NMA within a voltage range of 2.8-4.5 V at a rate current of 0.1C. **c**, Cycling performance of NM82, NMT, NMM and NMA within a 2.8-4.5 V voltage range at a rate current of *C*/3 with capacity retentions of 86.2, 87.3, 88.2 and 92.1%, respectively.

entirely transitions to a spinel-like and rock-salt structure. This indicates that oxygen release not only occurred on the surface, but also extended into the bulk. Identical characterization tests on bulk NM64 (Supplementary Fig. 22) showed that the morphological damage and irreversible phase transition were absent from the NM64 bulk even after 100 cycles, which proves that oxygen stability was substantially improved.

Observations (Fig. 6a-c) indicate that the NC64 surface structures completely changed to a rock-salt phase after prolonged cycling^{35,36}. This process was also observed on the NM64 sample (Fig. 6f-h), which suggests that surface phase transformation was independent of the Co and Mn content. The rock-salt phase was inevitably generated on the particle surface due to a reduction of surface Ni⁴⁺ reactions with the electrolyte accompanied by CO₂ generation. When making subsurface observations, the structural evolutions of NC64 and NM64 during the cycling presented a clear deviation. The subsurface structure of NC64 completely transited to a Co₃O₄-type spinel-like structure (Fig. 6a,d,e). Such an irreversible phase transition is related to oxygen release, which triggers TM migration to form a spinel-like phase^{37–39}. By comparison, the structure stability of NM64 was superior. Despite increased Li/Ni disorder, bulk NM 64 remained a typical layered structure after 100 cycles, which indicates that the Co reduction and Mn substitution improved the stability of the structure and oxygen of Ni-rich cathodes (Fig. 6f,i,j).

To further clarify this, electron energy-loss spectroscopy linescan spectra was conducted to compare the reversibility of the O redox and valance evolution of TMs. As shown in Fig. 6l and Supplementary Fig. 23a,b, the O K-edge pre-peak only decreased near the surface of NM64, and the L edges of Ni and Mn also consistently showed leftward shifts near the surface. These results suggest that oxygen release only occurred on surface areas of the NM64 particles. As a comparison, oxygen released not only occurred on the surface, but also extended into bulk NC64, because the O K-edge pre-peak of NC64 exhibited a relatively low intensity in the whole scan area of around 40 nm (Fig. 6k and Supplementary Fig. 23c,d). In addition, we compared the Ni L edges of bulk NC64 and NM64 (Supplementary Fig. 24). It was observed that the valance state of Ni in bulk NC64 was lower than that of bulk NM64, which indicates that the Ni valence states in NC64 decreased notably with more severe oxygen release. Based on the above discussion, Co is determined to be detrimental to structural/morphological stability and oxygen reversibility. Co reduction and Mn increase could greatly alleviate these challenges in Ni-rich cathodes.

Developing Ni-rich and Co-free cathodes

A comparison of the effects of Co and Mn substitution on capacity degradation is summarized in Fig. 7. Co effectively suppressed the formation of Li/Ni disorder, but in turn triggered huge lattice parameter changes and intergranular microcracks in single particles. Moreover, Co continuously activated unstable O redox, which caused oxygen release and irreversible phase transitions from layered to spinel-like structures. Together, these two factors predominately determined the capacity-degradation mechanism of Co-rich cathodes. In contrast, reducing Co with Mn substitution

was beneficial for the structural stability and suppression of oxygen release. As the pillar function of Li/Ni disorder, intergranular microcracks and irreversible phase transitions were absent from Co-free cathodes. The surface phase transformation from a layer structure to a rock-salt phase was confirmed as independent from the Co and Mn composition. Although Co reduction is taken for granted as an intuitive and natural way forward for a sustainable development of the cathode, our findings in this work pinpoint the roles of Co, and in doing so prove that a Co reduction could even be beneficial for a cathode performance improvement. Moreover, appropriate amounts of Li/Ni disorder (an approximate range of 3–7%) were found to improve the structural stability in Ni-rich cathode materials.

To further reinforce these important findings, we developed in this work two Co-free cathodes, ${\rm LiNi_{0.7}Mn_{0.3}O_2}$ (NM73) and ${\rm LiNi_{0.8}Mn_{0.2}O_2}$ (NM82), which provided promising performance results (Supplementary Table 5 and Supplementary Figs. 25–28). Notably, NM82 simultaneously exhibited a high capacity of 209 mAh g $^{-1}$, an outstanding cycle stability in both half cells and full cells at a high potential of 4.5 V and an improved thermal stability (Figs. 8b,c and Supplementary Figs. 7 and 29). All these are very competitive against the commercially available ${\rm LiNi_{0.8}Mn_{0.1}Co_{0.1}O_2}$ (NMC811) and ${\rm LiNi_{0.8}Co_{0.15}Al_{0.05}O_2}$ (NCA), but with a reduced material cost.

Motivated by the demonstrated successful NC82 doping to produce NCA 40 , these superior qualities of Co-free cathodes deserve further optimization to continuously enhance electrochemical performance. We further propose a series of compositional phases, $\text{LiNi}_\alpha \text{Mn}_\beta X_\gamma O_2$ (X = single or multiple dopants). X can be selected or combined purposefully from previously proved elements to achieve multifunctional improvements, which include structural stability, cycle performance at high potentials and electronic and/or ionic conductivity. Successful candidates provided here (Fig. 8b,c), such as $\text{LiNi}_{0.79}\text{Mn}_{0.2}\text{Mg}_{0.01}O_2$ (NMM), $\text{LiNi}_{0.79}\text{Mn}_{0.2}\text{Ti}_{0.01}O_2$ (NMT) and $\text{LiNi}_{0.8}\text{Mn}_{0.15}\text{Al}_{0.05}O_2$ (NMA), show high capacities of 210 mAh g $^{-1}$ and a high voltage functionality (4.5 V), which Co-reliant Ni-rich cathodes hardly reach, which reinforces the practicality of Co-free cathode materials.

Other feasible strategies include surface coating and concentration-gradient designs that can potentially suppress the surface reactivity and extend cycle life of Co-free cathodes. We believe that, with further modification, Co-free cathodes are promising candidates to replace the current NMC and NCA cathodes and will play a critical role in accelerating widespread vehicle electrification.

Conclusions

With state-of-the-art techniques, we thoroughly investigated the intrinsic properties of Co and/or Mn content and the impact of Co reduction, which included Co free, on Ni-rich cathode materials. Although high Ni contents were previously recognized as the origin of capacity degradation, we found that Co is more destructive than Ni at high potentials and the undeniable cause for the structural instability and capacity decay. Our results further suggest that the presence of Co suppresses Li/Ni disorder, exacerbates lattice parameter changes and promotes the formation of intragranular microcracks. Meanwhile, Co-rich contents excessively trigger irreversible lattice O redox, which induces oxygen release and irreversible structural transformation. These morphological and structural degradation mechanisms are identified as the root cause of the accelerated capacity decay observed in Co-rich cathodes. Furthermore, we attribute the use of Mn in Co-free cathodes to lattice O stabilization and the suppression of irreversible phase transitions during cycling, despite the increases in Li/Ni disorder. Thus, the Mn substitution in Ni-rich cathodes could be capable of high-voltage operations. Inspired by these fundamental understandings, we report a series of practical Co-free cathodes, represented as LiNi_αMn_βX_νO₂, that exhibit encouraging performances and hold promise for use in long-cycle-life batteries and future commercial applications.

Methods

Materials synthesis. The single-particle precursors of Ni $_{0.6}$ Mn $_{0.4}$ (OH) $_2$, Ni $_{0.6}$ Co $_{0.4}$ (OH) $_2$, Ni $_{0.6}$ Mn $_{0.2}$ Co $_{0.2}$ (OH) $_2$ and Ni $_{0.8}$ Co $_{0.2}$ (OH) $_2$ and the secondary particle precursor of Ni $_{0.8}$ Mn $_{0.2}$ (OH) $_2$ were all synthesized via a co-precipitation method. Appropriate amounts of NiSO $_4$ ·6H $_2$ O, CoSO $_4$ ·7H $_2$ O and MnSO $_4$ ·H $_2$ O were used as the starting materials for the [Ni $_8$ Mn $_9$ Co $_2$](OH) $_2$ synthesis. For single particle precursors, a mixed aqueous solution of Ni, Co and Mn with a concentration of 1.0 moll $^{-1}$ was pumped into a homemade continuously stirred tank reactor (11) under a N $_2$ atmosphere. Concurrently, a 4.0 moll $^{-1}$ NaOH solution (aqueous) and the desired amounts of NH $_4$ OH solution (aqueous) as a chelating agent were separately pumped into the reactor. The pH value of the precursor solution was kept at 10, the temperature at 60 °C and the stirring speed at 500 r.p.m.

A commercial 4l continuously stirred tank reactor was employed to synthesize the secondary particle precursors of NM73, NM82 and NMA. A starting solution mixture of Ni, Mn and Al at 2.0 moll⁻¹ was pumped into the reactor under a N₂ atmosphere. At the same time, a 4.0 moll⁻¹ NaOH solution (aqueous) and 5.0 moll⁻¹ NH₄OH solution (aqueous), which acted as a chelating agent, was also pumped into the reactor. The pH value of the precursor solution was kept at 10.5–11, the temperature at 60 °C and the stirring speed at 1,000 r.p.m.

The precursor powders were obtained after filtering, washing and vacuum drying in an oven overnight. LiNi $_{0.6}$ Co $_{0.4}$ O $_{2}$. LiNi $_{0.6}$ Mn $_{0.2}$ Co $_{0.2}$ O $_{2}$. LiNi $_{0.6}$ Mn $_{0.4}$ O $_{2}$. LiNi $_{0.8}$ Mn $_{0.2}$ O $_{2}$ O $_{2}$. LiNi $_{0.6}$ Mn $_{0.4}$ O $_{2}$. LiNi $_{0.8}$ Mn $_{0.2}$ O $_{2}$ O $_{2}$. LiNi $_{0.8}$ Mn $_{0.2}$ O $_{2}$ O $_{2}$. LiNi $_{0.8}$ Mn $_{0.2}$ O $_{2}$ O $_{2}$ were prepared by thoroughly mixing the corresponding precursors with the appropriate contents of LiOH·H $_{2}$ O (in a molar ratio of Li·TM = 1.03:1). LiNi $_{0.7}$ Mn $_{0.2}$ Mg $_{0.0}$ O $_{2}$ and LiNi $_{0.7}$ Mn $_{0.2}$ Ti $_{0.0}$ O were prepared by mixing the Ni $_{0.8}$ Mn $_{0.2}$ O(H) $_{2}$ precursors with nanosized MgO and TiO $_{2}$ first, and then mixing with the appropriate contents of LiOH·H $_{2}$ O (in a molar ratio of Li·TM = 1.03:1). Thereafter, the mixtures were calcinated at various temperatures for 12h under an oxygen atmosphere: 780 °C for LiNi $_{0.6}$ Co $_{0.4}$ O $_{2}$, 800 °C for LiNi $_{0.6}$ Mn $_{0.2}$ Co $_{0.2}$ O $_{2}$, 850 °C for LiNi $_{0.6}$ Mn $_{0.4}$ O $_{2}$, 750 °C for LiNi $_{0.8}$ Co $_{0.2}$ O $_{2}$, 825 °C for LiNi $_{0.8}$ Mn $_{0.2}$ Co $_{0.2}$ O $_{2}$, 800 °C for LiNi $_{0.8}$ Mn $_{0.15}$ Al $_{0.05}$ O $_{2}$, 800 °C for LiNi $_{0.7}$ Mn $_{0.2}$ Mn $_{0.2}$ O $_{2}$ and 800 °C for LiNi $_{0.7}$ Mn $_{0.2}$ Mn $_{0.2}$ O $_{2}$ and 800 °C for LiNi $_{0.7}$ Mn $_{0.2}$ Mn $_{0.2}$ O $_{2}$ and 800 °C for LiNi $_{0.7}$ Mn $_{0.2}$ Mn $_{0.2}$ O $_{2}$ and 800 °C for LiNi $_{0.7}$ Mn $_{0.2}$ Mn $_{0.2}$ O $_{2}$ and 800 °C for LiNi $_{0.7}$ Mn $_{0.2}$ Mn $_{0.2}$ O $_{2}$ and 800 °C for LiNi $_{0.7}$ Mn $_{0.2}$ Mn $_{0.2}$ O $_{2}$ and 800 °C for LiNi $_{0.7}$ Mn $_{0.2}$ Mn $_{0.2}$ O $_{2}$ and 800 °C for LiNi $_{0.7}$ Mn $_{0.2}$ Mn $_{0.2}$ O $_{2}$ and 800 °C for LiNi $_{0.7}$ Mn $_{0.2}$ Mn $_{0.2}$ O $_{2}$ and 800 °C for LiNi $_{0.7}$ Mn $_{0.2}$ Mn $_{0.2}$ O $_{2}$ and 800 °C for LiNi $_{0.7}$ Mn $_{0.2}$ O $_{2}$ and 800 °C for LiNi $_{0.7}$ Mn $_{0.2}$ O $_{2}$ and 800 °C for LiNi $_{0.7}$ Mn $_{0.2}$ O $_{2}$ and 800 °C for LiNi $_{0.7}$ Mn $_{0.7}$ O $_{2}$ and 800 °C for LiNi $_{0.7}$ Mn $_{0.7}$ O $_{2}$ Mn $_{2}$ O $_$

Electrochemical tests. For electrochemical testing, active materials were mixed with carbon black and PVDF at 80:10:10 wt% ratios and ground in a mortar. 2032 type coin cells were used to prepare lithium half cells. Celgard 2325 separators and 1.2 M LiPF₆ in EC / EMC (3:7) electrolyte (GEN II) were used. The half cells were then cycled between 2.8 and 4.5 V s Li+/Li, using small amounts of powder (\sim 5.2 mg/cm²) as positive electrodes. For the full cell, a 2032-coin cell was assembled using high loading cathode (\sim 12.8 mg/cm²) and graphite anode and then cycled within a voltage range of 2.8 and 4.45 V. The N/P ratio for the full cell was around 1.2 and commercial graphite was provided by Shenzhen BTR New Energy Materials Inc.

Synchrotron X-ray measurements. Data for the cathode materials was collected using HEXRD located at sector 11-ID-C of the Advanced Photon Source at Argonne National Laboratory. A high-energy X-ray with a beam size of $0.2\,\mathrm{mm}\times0.2\,\mathrm{mm}$ and wavelength of $0.1173\,\mathrm{\mathring{A}}$ was used to obtain two-dimensional diffraction patterns in the transmission geometry. X-ray patterns were recorded with a Perkin-Elmer large-area detector placed $1,800\,\mathrm{mm}$ from the samples. Rietveld refinements of the collected HEXRD patterns were carried out using the GSAS package.

In situ time-resolved high-energy synchrotron XRD measurements during cycling were performed at the same beamline. With a high penetration and low absorption, synchrotron HEXRD precisely reflects bulk sample structure properties in real time and realistic conditions. This is beneficial when observing tiny phase changes that usually are invisible from lab-scale XRD due to poor background noise and time-limited resolutions. The 2032 coin cells exhibited a 3 mm hole suitable for X-rays to pass through and diffraction patterns were collected every 10 min.

XANES for the Ni K edge, Mn K edge and Co K edge were performed at the Advanced Photon Source on the bending-magnet beamline 9-BM-B. The X-ray photon energy was monochromatized by an Si(111) double-crystal monochromator. Higher-order harmonic contaminations were eliminated by detuning the monochromator to reduce the incident X-ray intensity by approximately 30%. All the spectra were collected at room temperature in the transmission mode.

Gas evolution analysis. Differential electrochemical mass spectrometry was applied to detect and identify the gas evolution of different cathode materials during first charge/discharge. A homemade cell with glass fibre separators and 1.2 M LiPF₆ in an ethyl carbonate/ethyl methyl carbonate (3:7) electrolyte (GEN II) was used for in situ measurements. The cells were then cycled at a current rate of C/10 between 2.8 and 4.5 V versus Li*/Li, using small amounts of powder (~5.2 mg cm⁻²) as the positive electrodes.

TEM measurement. High-resolution TEM images of all the cathode materials were conducted on a FEI Titan 80-300ST with a spherical and chromatic aberration imaging corrector.

Data availability

All the relevant data are included in the paper and its Supplementary Information.

Received: 3 March 2020; Accepted: 24 December 2020; Published online: 18 February 2021

References

- Wang, X., Ding, Y. L., Deng, Y. P. & Chen, Z. Ni-rich/Co-poor layered cathode for automotive Li-ion batteries: promises and challenges. *Adv. Energy Mater.* 10, 1903864 (2020).
- Li, H. et al. Is cobalt needed in Ni-rich positive electrode materials for lithium ion batteries? J. Electrochem. Soc. 166, A429–A439 (2019).
- Olivetti, E. A., Ceder, G., Gaustad, G. G. & Fu, X. Lithium-ion battery supply chain considerations: analysis of potential bottlenecks in critical metals. *Joule* 1, 229–243 (2017).
- Bessette, S. et al. Nanoscale lithium quantification in Li_xNi_yCo_wMn_zO₂ as cathode for rechargeable batteries. Sci. Rep. 8, 1–9 (2018).
- Zhang, J.-N. et al. Trace doping of multiple elements enables stable battery cycling of LiCoO₂ at 4.6 V. Nat. Energy 4, 594–603 (2019).
- Tsai, P. C. et al. Single-particle measurements of electrochemical kinetics in NMC and NCA cathodes for Li-ion batteries. *Energy Environ. Sci.* 11, 860–871 (2018).
- 7. Li, M. & Lu, J. Cobalt in lithium-ion batteries. Science 367, 979-980 (2020).
- Hu, E. et al. Evolution of redox couples in Li- and Mn-rich cathode materials and mitigation of voltage fade by reducing oxygen release. *Nat. Energy* 3, 690–698 (2018).
- Liu, T. et al. Correlation between manganese dissolution and dynamic phase stability in spinel-based lithium-ion battery. Nat. Commun. 10, 4721 (2019).
- Li, W. et al. Enabling high areal capacity for Co-free high voltage spinel materials in next-generation Li-ion batteries. J. Power Sources 473, 228579 (2020).
- 11. Lee, J. et al. Unlocking the potential of cation-disordered oxides for rechargeable lithium batteries. *Science* **343**, 519–522 (2014).
- Liu, C., Neale, Z. G. & Cao, G. Understanding electrochemical potentials of cathode materials in rechargeable batteries. *Mater. Today* 19, 109–123 (2016).
- Schipper, F. et al. Review—recent advances and remaining challenges for lithium ion battery cathodes. J. Electrochem. Soc. 164, A6220–A6228 (2016).
- Yan, P. et al. Tailoring grain boundary structures and chemistry of Ni-rich layered cathodes for enhanced cycle stability of lithium-ion batteries. Nat. Energy 3, 600–605 (2018).
- Mu, L. et al. The sensitive surface chemistry of Co-free, Ni-rich layered oxides: identifying experimental conditions that influence characterization results. J. Mater. Chem. A 8, 17487–17497 (2020).
- Kaboli, S. et al. Behavior of solid electrolyte in Li-polymer battery with NMC cathode via in-situ scanning electron microscopy. *Nano Lett.* 20, 1607–1613 (2020).
- 17. Xiao, Y. et al. Insight into the origin of lithium/nickel ions exchange in layered Li(Ni_xMn_yCo_z)O₂ cathode materials. *Nano Energy* **49**, 77–85 (2018).
- Zou, Y. et al. Multishelled Ni-rich Li(Ni_xCo_pMn_z)O₂ hollow fibers with low cation mixing as high-performance cathode materials for Li-ion batteries. Adv. Sci. 4, 1600262 (2017).
- Zheng, J. et al. Ni/Li disordering in layered transition metal oxide: electrochemical impact, origin, and control. Acc. Chem. Res. 52, 2201–2209 (2019).
- Zheng, Z. et al. Thermodynamically revealing the essence of order and disorder structures in layered cathode materials. *Chin. J. Struct. Chem.* 38, 2020–2026 (2019).
- Zhao, J. Q. et al. In situ probing and synthetic control of cationic ordering in Ni-rich layered oxide cathodes. Adv. Energy Mater. 7, 1601266 (2017).
- Zhao, E. Y. et al. New insight into Li/Ni disorder in layered cathode materials for lithium ion batteries: a joint study of neutron diffraction, electrochemical kinetic analysis and first-principles calculations. *J. Mater. Chem. A* 5, 1679–1686 (2017).
- Duan, Y. D. et al. Insights into Li/Ni ordering and surface reconstruction during synthesis of Ni-rich layered oxides. J. Mater. Chem. A 7, 513–519 (2019).
- Zhang, M. J. et al. Cationic ordering coupled to reconstruction of basic building units during synthesis of high-Ni layered oxides. *J. Am. Chem. Soc.* 140, 12484–12492 (2018).
- Kang, K. S., Meng, Y. S., Breger, J., Grey, C. P. & Ceder, G. Electrodes with high power and high capacity for rechargeable lithium batteries. *Science* 311, 977–980 (2006).
- 26. Li, H., Zhang, N., Li, J. & Dahn, J. R. Updating the structure and electrochemistry of Li_xNiO₂ for 0 ≤ x ≤1. *J. Electrochem. Soc.* 165, A2985–A2993 (2018).
- 27. Ryu, H.-H., Park, K.-J., Yoon, C. S. & Sun, Y.-K. Capacity fading of Ni-rich Li[Ni_xCo_yMn_{1-x-y}]O₂ (0.6≤x≤0.95) cathodes for high-energy-density lithium-ion batteries: bulk or surface degradation? *Chem. Mater.* **30**, 1155–1163 (2018).

- Zeng, X., Zhan, C., Lu, J. & Amine, K. Stabilization of a high-capacity and high-power nickel-based cathode for Li-ion batteries. Chem 4, 690–704 (2018).
- Jung, R., Metzger, M., Maglia, F., Stinner, C. & Gasteiger, H. A. Oxygen release and its effect on the cycling stability of LiNi_xMn_yCo₂O₂ (NMC) cathode materials for Li-ion batteries. *J. Electrochem. Soc.* 164. A1361–A1377 (2017).
- Li, N. et al. Unraveling the cationic and anionic redox reactions in a conventional layered oxide cathode. ACS Energy Lett. 4, 2836–2842 (2019).
- Assat, G. & Tarascon, J. M. Fundamental understanding and practical challenges of anionic redox activity in Li-ion batteries. *Nat. Energy* 3, 373–386 (2018).
- Yan, P. et al. Injection of oxygen vacancies in the bulk lattice of layered cathodes. Nat. Nanotechnol. 14, 602–608 (2019).
- Yan, P. et al. Intragranular cracking as a critical barrier for high-voltage usage of layer-structured cathode for lithium-ion batteries. *Nat. Commun.* 8, 14101 (2017).
- 34. Lin, F. et al. Metal segregation in hierarchically structured cathode materials for high-energy lithium batteries. *Nat. Energy* 1, 1–8 (2016).
- Lin, F. et al. Surface reconstruction and chemical evolution of stoichiometric layered cathode materials for lithium-ion batteries. *Nat. Commun.* 5, 3529 (2014).
- 36. Sun, H.-H. & Manthiram, A. Impact of microcrack generation and surface degradation on a nickel-rich layered Li[Ni_{0.9}Co_{0.05}Mn_{0.05}]O₂ cathode for lithium-ion batteries. *Chem. Mater.* 29, 8486–8493 (2017).
- Gent, W. E. et al. Coupling between oxygen redox and cation migration explains unusual electrochemistry in lithium-rich layered oxides. *Nat. Commun.* 8, 2091 (2017).
- House, R. A. et al. What triggers oxygen loss in oxygen redox cathode materials? Chem. Mater. 31, 3293–3300 (2019).
- 39. Lee, W. et al. Advances in the cathode materials for lithium rechargeable batteries. *Angew. Chem. Int. Ed.* **58**, 2–30 (2019).
- Chen, C. H. et al. Aluminum-doped lithium nickel cobalt oxide electrodes for high-power lithium-ion batteries. J. Power Sources 128, 278–285 (2004).

Acknowledgements

We acknowledge support from the US Department of Energy (DOE), Office of Energy Efficiency and Renewable Energy (EERE), Vehicle Technologies Office (VTO). This work was also supported by Clean Vehicles, US-China Clean Energy Research Centre (CERC-CVC2) under the US DOE EERE Vehicle Technologies Office. Argonne National Laboratory is operated for the DOE Office of Science by the UChicago Argonne, LLC, under contract no. DE-AC02-06CH11357. This research was partially supported by the National Key R&D Program of China (2016YFB0700600), the Guangdong Innovation Team Project (no. 2013N080), the Soft Science Research Project of Guangdong Province (no. 2017B030301013) and the Shenzhen Science and Technology Research Grants (no. ZDSYS201707281026184). T.L. thanks F.P. for the supervision and consultation on this work during his PhD study. This research used resources of the Advanced Photon Source (11-ID-C and 9-BM), a US Department of Energy (DOE) Office of Science User Facility operated for the DOE Office of Science by Argonne National Laboratory under Contract no. DE-AC02-06CH11357. This work was performed including electron microscopy, in part, at the Center for Nanoscale Materials, a US Department of Energy Office of Science User Facility, and supported by the US Department of Energy, Office of Science, under Contract no. DE-AC02-06CH11357.

Author contributions

T.L., J. Lu, K.A. and F.P. conceived the idea and designed the experiments. T.L., Maofan Li and J. Liu synthesized all the materials. T.L. and Y.R. carried out the in situ and ex situ synchrotron XRD results. T.L., L.M. and T.W. performed ex situ synchrotron XAS. Z.H., J.Z. and F.P. conducted the density functional theory calculations. T.L., A.D., Matthew Li and X.B. carried out the electrochemical measurements and analysis. L.Y., D.L. and J.W. conducted the TEM measurements. T.L., A.D., J. Lu, K.A and F.P. wrote the manuscript and all the authors edited the manuscript.

Competing interests

The authors declare no competing interests.

Additional information

Supplementary information The online version contains supplementary material available at https://doi.org/10.1038/s41560-021-00776-y.

Correspondence and requests for materials should be addressed to J.L., F.P. or K.A.

Peer review information *Nature Energy* thanks Xinping Ai and the other, anonymous, reviewer(s) for their contribution to the peer review of this work.

Reprints and permissions information is available at www.nature.com/reprints.

Publisher's note Springer Nature remains neutral with regard to jurisdictional claims in published maps and institutional affiliations.

@ UChicago Argonne, LLC, Operator of Argonne National Laboratory under exclusive licence to Springer Nature Limited 2021